Communication

Journal of Photopolymer Science and Technology
Volume 36, Number 5 (2023) 373−378 ©2023SPST

Electron Generation in Tin-oxo Cage Extreme Ultraviolet Photoresists

Najmeh Sadegh[1], Quentin Evrard[1,2], Nicola Mahne[3], Angelo Giglia[3], Stefano Nannarone[3] and Albert M. Brouwer[1,2*]

[1] Advanced Research Center for Nanolithography, Science Park 106, 1098 XG, Amsterdam, The Netherlands
[2] van 't Hoff Institute for Molecular Sciences, University of Amsterdam, Science Park 904, 1098 XH Amsterdam, The Netherlands
[3] IOM-CNR, 34149 Basovizza, Trieste, Italy
**a.m.brouwer@uva.nl*

Extreme Ultraviolet Lithography photoresists undergo chemical reactions initiated by ionizing radiation. Understanding the decay pathways in the photoresist following photoionization requires knowledge about the states and species that are generated during the ultrafast primary and secondary ionization processes while the energy of the photons (92 eV) is ultimately converted to heat and chemical reaction products. Here we use Total Electron Yield spectroscopy to investigate the electron generation following excitation of the resist with photons in the energy range from 5 to 150 eV. We estimate that each EUV photon gives rise to 3 – 4 electrons. Changes in the material during irradiation lead to changes in the yield of electrons, which is qualitatively explained by considering changes in the absorption spectrum and density that are due to chemical change.
Keywords: Extreme ultraviolet, Photoresist, Total Electron Yield, Organotin compound

1. Introduction

In the past few years, Extreme Ultraviolet Lithography has made the transition from the development stage to increasingly large-scale production [1]. Further development of the hardware follows a programmed route towards higher numerical apertures [2], but for the chemical software of photolithography, the photoresist, the pathway for improvement is less obvious. The chemically amplified resist (CAR) materials originally developed for 193 nm photolithography have been adapted for use with the 13.5 nm photon source, but the limitations of this approach have been pointed out: being organic polymer based, CARs have low absorption cross sections at 13.5 nm and their etch resistance may be insufficient when used in the thin layers that are required in small-sized patterns with a reasonably small aspect ratio [3]. As an alternative, metal-containing materials have been proposed, and they have been under investigation for more than a decade now [4,5].

From a more fundamental perspective, the development of EUV photoresists is hampered by a lack of knowledge and understanding of the chemistry induced by the ionizing radiation used. Photons with an energy of 92 eV cause the emission of photoelectrons from valence and shallow-core orbitals. These electrons, which may have kinetic energies up to ~85 eV, can cause further ionizations, generating a number of secondary electrons. It is often stated that the electrons are responsible for radiation induced chemistry, but a clear mechanistic picture is available only in few cases [6–8]. From the perspective of pattern fidelity, the secondary electrons raise the same questions as acids in CAR: to what extent do they blur the pattern projected in the areal image?

In our research we have investigated tin-oxo cages as a prototype material for EUV resist application. These have been introduced in the field by the Brainard group [9], and it has been suggested that they form the basis of the photoresists commercially developed by Inpria [10–12].

One aspect of the chemistry of these compounds

Received May 14, 2023
Accepted June 5, 2023

(and related organotin compounds) is clear: any form of activation, be it UV, XUV or EUV photons, or electrons (even of low energy), leads to the cleavage of tin-carbon bonds [13–20]. Unfortunately, direct experimental evidence for the molecular structure of the subsequent reaction products is lacking. We have detected photofragmentation products, which lost multiple butyl groups from the original *n*-butyltin-oxo cages, and proposed structures based on quantum-chemical calculations [21]. It is likely that the cages after loss of the alkyl groups cross-link to form higher molecular weight chains or cross-linked networks that are insoluble, but there is no experimental evidence for the chemical nature of the bonds between cages [11]. The main reason for this is that available spectroscopic methods lack the specificity and sensitivity to give the required quantitative insight. The problem is aggravated by the fact that only a relatively small conversion is needed to achieve the solubility switching, and that the spectroscopic signatures of the different bond types do not change much when few of the carbon-tin bonds are broken while most remain intact.

In previous work, we studied the photoelectron spectrum of different tin-oxo cages with photon energies in the range 60 – 150 eV, which showed that the ratio of Sn(4d) electrons to valence electrons has a maximum near a photon energy of 92 eV [22].

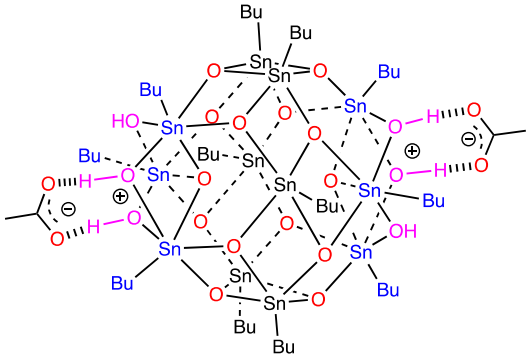

Scheme 1. Molecular structure of the TinOAc photoresist material investigated.

In the present work we describe Total Electron Yield (TEY) measurements in which we scan the photon energy over the much wider range from 5 to 150 eV and detect the total electron emission rate (drain current) from the sample, which results from the photoemission at the surface of the thin resist film.[23]

By comparing the shape of this TEY spectrum to the absorption spectrum, we obtain information on the electron yield as a function of the photon energy. Because the irradiation leads to chemical change, the TEY changes during the measurement. Time traces of the electron yield vs. exposure dose reveal different responses in the low and high energy ranges.

2. Experimental

The TinOAc photoresist was prepared as described before [16]. Films with a thickness of ~20 nm were spin-coated on silicon substrates (2 × 2 cm^2) from toluene solutions (10 mg/mL).

Total Electron Yield measurements (TEY) were performed at the BEAR beamline of Synchrotron Elettra, Trieste, Italy [24]. The polarization of the synchrotron beam can be set, the wavelength monochromatized and filtered to remove higher orders contributions before being focused on the sample. The drain current generated in the refocusing mirror acts as continuous intensity monitor. It is used to normalize the incoming intensities and related signals among runs taken at different times.

To cover the whole photon energy range of interest (5 – 150 eV), two 1200 lines/mm gratings were used differing in monochromator inclusion angle. The photon beam was linearly polarized in the horizontal synchrotron orbit plane impinging at 45° in *s* (*TE*) incidence. The vertical slit of the monochromator in the dispersive plane was set to 50 μm, to ensure a band pass <0.1 eV. The horizontal slit width was 890 μm. The spot size on the sample was ~70 × 320 μm^2 (vertical × horizontal). A -5 V bias was applied to the sample to maximize emission current signal.

To determine the electron yield, the current from the sample was measured. The TEY is obtained in electrons per photons as the ratio of rate of emitted electrons (derived from the drain current signal) to the rate of impinging photons obtained from the current signal of a calibrated photodiode inserted into the photon beam at different instant of time, then renormalizing the signals through the corresponding monitor signals from the mirror.

Because the photoresist sample is inherently radiation sensitive, for each photon energy a fresh unexposed spot on the sample was selected. Multiple acquisition is performed at each point to follow the time evolution of the TEY. The TEY spectrum presented in Fig.1 is composed of the data in the first time interval. By monitoring the signal over time, the effect of the radiation induced chemical change was detected.

3. Results and discussion

3.1. TEY spectrum

A representative Total Electron Yield spectrum of TinOAc on silicon is shown in Figure 1.

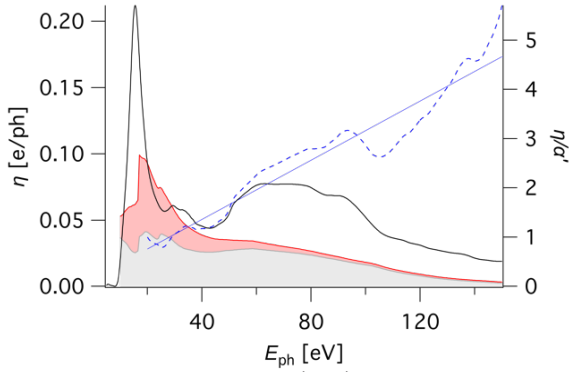

Fig. 1. TEY spectrum $\eta(E_{\mathrm{ph}})$ of TinOAc (black) plotted together with the absorption spectrum (red), scaled to the same value at 20 eV, their ratio η/α' (blue dashed line) and a linear fit of the ratio vs. photon energy. The grey area is the unbleachable part of the absorption, the red area the bleachable part (see ref. [25]).

3.2. Time traces of the TEY

The TEY values shown in Fig. 1 were obtained for each energy from 0.5 s of data acquisition and ~2 s of exposure at a fresh point on the sample. The same spots were irradiated for 120 time intervals of ~2 s, which reveals the effect of the chemical change of the resist film under the influence of the radiation on the detected electron yield. As shown in Fig. 2, in the low photon energy regime, an initial decrease of the signal is observed, followed by a recovery. At energies near 100 eV the signal increases from the beginning of the irradiation.

3.3. Discussion

Spectral features. In fig. 1 the TEY spectrum of TinOAc is shown together with the absorption spectrum derived from the cross sections in the CXRO database [26]. As we have recently shown, this predicted spectrum is in very good agreement with the experimental data obtained by absorption and photobleaching experiments in the XUV range [25,27].

The onset of the TEY spectrum occurs near 8 eV constituting an indication of the value of the ionization energy. At this energy electrons originating from the highest occupied molecular orbitals (HOMO) can reach the vacuum level and be emitted into vacuum.

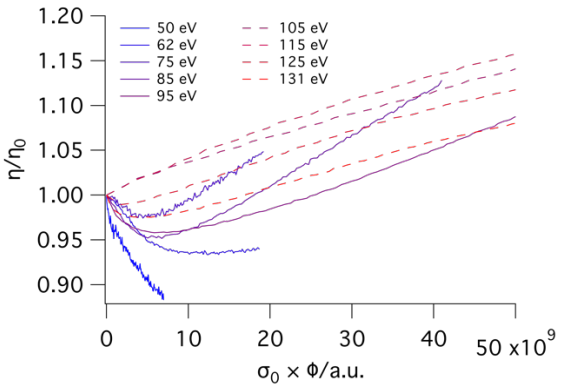

Fig. 2. Representative time traces of the TEY signal for selected photon energies. The horizontal axis displays the cumulative number of photons on the sample at the given photon energy multiplied by the absorption cross section at t = 0. The length of the traces is limited by the photon flux, which is low in the range <80 eV and peaks near 120 eV.

Since the HOMO-LUMO gap is ~5 eV, the electron affinity must be ~3 eV. In gas phase photofragmentation experiments we found the onset of ionization at 12 eV for the bare tin-oxo cage dication, and at 10 eV for a tin-oxo dication complexed with one monovalent counter-anion [21]. The electrostatic effect of adding the second counterion together with the dielectric effect of the matrix is responsible for another 2 eV shift.

The strongest peak in the spectrum is found at ~15.5 eV. In this energy range, a high density of electronically excited valence (σ*) and Rydberg states co-exists with ionized states. We tentatively attribute the strong TEY signal to efficient autoionization. Note that at hν <20 eV the CXRO predictions are not reliable because the high-energy valence transitions cannot be considered as purely atomic transitions. Thus, the low-energy peak in the TEY spectrum with its maximum at 15.5 eV should not be compared with the CXRO spectrum.

Strong absorption giving rise to ionization from the Sn(4d) level (binding energy ~29 eV) kicks in around 50 eV and is responsible for the broad band that extends up to ~100 eV.

Changes of TEY during exposure. As mentioned in the introduction, the characteristic radiation-induced chemical process in organotin-oxo cages is the loss of the hydrocarbon substituents due to breaking of the tin-carbon bonds. In a recent study we found that broadband XUV irradiation leads to a loss of 60-70% of the cleavable organic groups (including acetate and water) [25,27]. This leads to a decrease of the absorption, especially in the low energy region. The bleachable and non-

bleachable parts of the absorption are shown in Fig. 1. Without attempting a quantitative analysis, we can use these spectral changes to tentatively account for the evolution of the TEY $\eta(E_{ph})$ with exposure. At lower energies, η initially decreases due to the chemical conversion. The decrease of the absorption cross section is responsible for this, as a smaller cross section means that photons penetrate more deeply into the material, to depths where photoelectrons cannot escape because of their limited mean free path. Moving to higher energies the photobleaching becomes less important because of the smaller contribution of carbon to the absorption (Fig. 1), and the effect of increased density due to the loss of the butyl groups becomes dominant. Around 105 eV the TEY signal increases from the beginning of the exposure. When the hydrocarbon fraction is reduced due to outgassing, the photon absorption occurs on average more closely to the surface, allowing more efficient escape of the photoelectrons.

A more detailed quantitative analysis will be presented in a future paper.

TEY spectrum and electron yield. Primary photoelectrons with higher kinetic energies can induce more secondary ionizations via inelastic scattering. For example, Arumainayagam et al. state that typically 40,000 electrons are produced per MeV of radiation deposited [28]. In other words, the average energy consumed per electron generated amounts to ~25 eV. TEY measurements are frequently used as an indirect semi-quantitative way of measuring X-ray absorption spectra [23]. In that case the total electron yield η is treated as proportional to the absorption factor $\alpha(E_{ph})$ and the photon energy E_{ph}:

$$\eta(E_{ph}) \propto \alpha(E_{ph}) \times E_{ph} \quad (1)$$

The absorption coefficient α is related to the cross section σ by the Lambert-Beer law $\alpha = \sigma z \rho / M$, in which z is the film thickness, ρ the density and M the molecular weight. For our analysis we use the cross sections from the CXRO database [26] which were recently shown to match very well with experimental data in the XUV range 22 – 92 eV.[25]

The process of secondary electron generation has been depicted as a cascade, in which a photoelectron generates secondary electrons, which in turn generate more electrons [29]. Based on our results and discussions in the literature, however, it appears more likely that the primary photoelectrons lose energy by inelastic scattering in preferred quantities that correspond to the plasmon energy [30], as illustrated in Scheme 2.

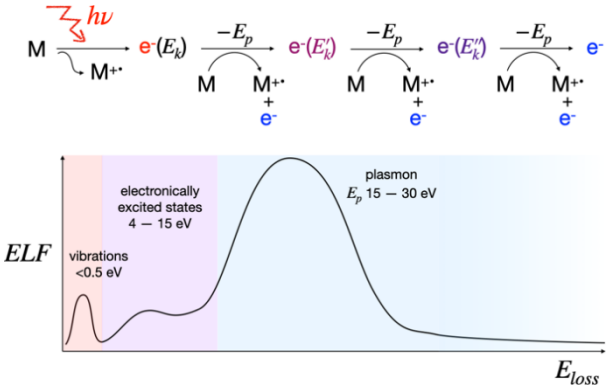

Scheme 2. Schematic representation of electron energy loss following valence excitation in the EUV range. Sketch of a typical Electron energy Loss Function (ELF), qualitatively indicating the energies and relative cross sections for the typical loss processes in molecular materials.

Among chemists, plasmons are well known as properties of metallic nanostructures, which give rise to visible absorption and light scattering [31]. More generally, plasmons occur in all materials as collective excitations of electrons. They are the most effective sink for the kinetic energy of electrons, that is, the plasmon dominates the electron energy loss function (ELF). Scheme 2 sketches the shape of a typical ELF for an organic material [32–34]. At the lowest loss energies, electrons can excite materials to higher vibrational energy levels. Next, electronic excitations are possible, and then in the range of 15 – 30 eV the plasmon loss can occur. Because this has a high cross section, electrons prefer to lose energy in amounts corresponding to the plasmon energy. In the low energy region additional loss mechanisms may play a role which lead to electron-induced reactions for example via dissociative electron attachment [35,36]. The excited plasmon dissociates to an electron hole pair, thus generating a low energy secondary electron [37].

When the ELF of a material is known, it is possible to simulate the decay of photoelectrons based on first principles, without any other experimental input.[30] Unfortunately, the electron energy loss function of the tin-oxo cage materials is unknown. An estimation of the plasmon energy, however, is provided by equation (2) [31].

$$E_p = \hbar \sqrt{\frac{ne^2}{\epsilon_0 m_e}} \quad (2)$$

In equation 2, n is the density of valence electrons,

e the electron charge, ε_0 the dielectric permittivity constant and m_e the electron mass. For poly(methylmethacrylate), equation 2 predicts E_p = 22 eV, in good agreement with experiment (E_p = 21 eV) [33]. For TinOAc, we find E_p = 27 eV, due to the higher valence electron density.

Although the proportionality in equation (1) is likely to break down at low energies, it is still interesting to consider its implications by comparing the measured TEY spectrum with the absorption spectrum. Considering that it takes E_{ph} >8 eV to liberate an electron from TinOAc, we assume that E_{ph} >20 eV is required to generate an electron that has enough energy to give rise to a secondary ionization with an appreciable probability. In Fig. 1 we plot the ratio η/α, scaled to η/α = 1 at 20 eV, vs. E_{ph} and fit a straight line according to eq. 1. The slope is 0.03 e/eV, and the value of η/α at 92 eV is ~3. This corresponds to an average energy loss of ~27 eV per electron generated. This result depends on the details of the assumption made. For example, setting the onset of secondary electron generation at 25 eV gives a slope of 0.038 and a yield of 3.7 electrons at 92 eV. As can be seen in Fig. 1, the ratio η/α vs. E_{ph} deviates substantially from a straight line. We plan to analyze these data in more detail in future work.

The above analysis applies to the valence electrons, which are emitted with a kinetic energy mostly in the range 75 – 85 eV [22]. Electrons originating from Sn(4d) orbitals will have a lower kinetic energy, and thus generate fewer secondary electrons. In this case, however, the hole created in the Sn(4d) level is likely filled via an Auger process that releases another low energy electron [38].

The TEY spectrum reveals the yields of electrons that escape from the material. This would be proportional to electrons generated inside the material if the mean free path (MFP) of all electrons is the same. Examples in the literature suggest that the MFP is only a few nm but increasing with decreasing kinetic energy in the range <100 eV. Especially below the plasmon energy, the scattering cross sections are smaller.

Finally, another challenge not yet met is to relate the electron yield to the chemical reaction efficiency. In principle a thermalized electron hole pair could give rise to more than one Sn-C bond splitting. Moreover, the inelastic scattering of the electrons can lead to the formation of chemically reactive electronically excited states [15,21], in addition to low energy electrons. On the other hand, several electron-hole pairs created in a small volume in the material can readily undergo recombination, and even after Sn-C bond cleavage, bond recombination is not unlikely, because the butyl radical cannot easily diffuse through the matrix. To investigate these ultrafast processes, time-resolved experiments are required.

4. Conclusion

Total Electron Yield spectra of thin films of an *n*-butyltin-oxo cage compound were studied in the photon energy range of 5 – 150 eV. The results suggest that at the EUV energy of 92 eV, 3 to 4 electrons could be generated. During exposure, hydrocarbon material is outgassed, which leads to opposing effects on the TEY: a decrease due to a decreasing absorption coefficient, an increase due to an increase of the density. In photon energy ranges where the contribution of the hydrocarbon fraction to the absorption is high, the decrease dominates; when the absorption by the tin-oxo core is relatively stronger, the TEY increases with conversion.

Our results are consistent with electron mean free paths of a few nm, but more work is needed to quantify the distances travelled by the primary and secondary photoelectrons.

Acknowledgement

This work was performed in part in the Advanced Research Center for NanoLithography (ARCNL), a public private partnership of the University of Amsterdam (UvA), the VU University Amsterdam (VU), the Dutch Research Council (NWO) and the semiconductor equipment manufacturer ASML. A part of the work was supported by Nippon Shokubai, Japan. This project has received funding from the European Union's Horizon 2020 research and innovation program under the Marie Skłodowska-Curie grant agreement number 722149 and contributes to the ELENA (Low energy ELEctron driven chemistry for the advantage of emerging NAno-fabrication method) European training network. The authors gratefully acknowledge Elettra Sincrotrone Trieste for beam time (proposals 20200400 and 20205228).

References

1. H. J. Levinson, *Jpn. J. Appl. Phys.* **61** (2022) SD0803.
2. C. Zahlten, P. Gräupner, J. van Schoot, P. Kuerz, J. Stoeldraijer, and W. Kaiser, *Proc. SPIE* **11177** (2019) 111770B.
3. L. Li, X. Liu, S. Pal, S. Wang, C. K. Ober, and E. P. Giannelis, *Chem. Soc. Rev.* **46** (2017) 4855.
4. C. Luo, C. Xu, L. Lv, H. Li, X. Huang, and W. Liu, *RSC Advances* **10** (2020) 8385.

5. T. Manouras, and P. Argitis, *Nanomaterials* **10** (2020) 1593.
6. A. M. Brouwer, *J. Photopolym. Sci. Technol.* **35** (2022) 81.
7. A. Narasimhan, L. Wisehart, S. Grzeskowiak, L. E. Ocola, G. Denbeaux, and R. L. Brainard, *J. Photopolym. Sci. Technol.* **30** (2017) 113.
8. T. Kozawa, and S. Tagawa, *Jap. J. Appl. Phys.* **49** (2010) 030001.
9. B. Cardineau, R. Del Re, M. Marnell, H. Al-Mashat, M. Vockenhuber, Y. Ekinci, C. Sarma, D. A. Freedman, and R. L. Brainard, *Microelectron. Eng.* **127** (2014) 44.
10. S. T. Meyers, D. A. Keszler, K. Jiang, J. Anderson, and A. Grenville, US9310684B2, (2016).
11. W. D. Hinsberg, and S. Meyers, *Proc. SPIE* **10146** (2017) 1014604.
12. C. D. Needham, A. Narasimhan, U. Welling, L. S. Melvin III, P. De Schepper, J. Wouters, J. Severi, D. De Simone, and S. Meyers, *Proc. SPIE* **11323** (2020) 113230G.
13. I. Bespalov, Y. Zhang, J. Haitjema, R. M. Tromp, S. J. van der Molen, A. M. Brouwer, J. Jobst, and S. Castellanos, *ACS Appl. Mater. Interfaces* **12** (2020) 9881.
14. Y. Zhang, J. Haitjema, M. Baljozovic, M. Vockenhuber, D. Kazazis, T. A. Jung, Y. Ekinci, and A. M. Brouwer, *J. Photopolym. Sci. Technol.* **31** (2018) 249.
15. Y. Zhang, J. Haitjema, X. Liu, F. Johansson, A. Lindblad, S. Castellanos, N. Ottosson, and A. M. Brouwer, *J. Micro/Nanolitho., MEMS, MOEMS* **16** (2017) 023510.
16. J. Haitjema, Y. Zhang, M. Vockenhuber, D. Kazazis, Y. Ekinci, and A. M. Brouwer, *J. Micro/Nanolitho., MEMS, MOEMS* **16** (2017) 033510.
17. J. T. Diulus, R. T. Frederick, D. C. Hutchison, I. Lyubinetsky, R. Addou, M. Nyman, and G. S. Herman, *ACS Appl. Nano Mater.* **3** (2020) 2266.
18. M. C. Sharps, R. T. Frederick, M. L. Javitz, G. S. Herman, D. W. Johnson, and J. E. Hutchison, *Chem. Mater.* **31** (2019) 4840.
19. J. T. Diulus, R. T. Frederick, M. Li, D. C. Hutchison, M. R. Olsen, I. Lyubinetsky, L. Árnadóttir, E. L. Garfunkel, M. Nyman, H. Ogasawara, and G. S. Herman, *ACS Appl. Mater. Interfaces* **11** (2019) 2526.
20. R. P. Oleksak, R. E. Ruther, F. Luo, J. M. Amador, S. R. Decker, M. N. Jackson, J. R. Motley, J. K. Stowers, D. W. Johnson, E. L. Garfunkel, D. A. Keszler, and G. S. Herman, *ACS Appl. Nano Mater.* **1** (2018) 4548.
21. J. Haitjema, L. Wu, A. Giuliani, S. Castellanos, L. Nahon, and A. M. Brouwer, *Phys.Chem.Chem.Phys* **23** (2021) 20909.
22. Y. Zhang, J. Haitjema, S. Castellanos, O. Lugier, N. Sadegh, R. Ovsyannikov, E. Giangrisostomi, F. O. L. Johansson, E. Berggren, A. Lindblad, and A. M. Brouwer, *Appl. Phys. Lett.* **118** (2021) 171903.
23. J. Stöhr, *NEXAFS Spectroscopy*, Springer, Berlin, Heidelberg, **1992**.
24. S. Nannarone, F. Borgatti, A. DeLuisa, B. P. Doyle, G. C. Gazzadi, A. Giglia, P. Finetti, N. Mahne, L. Pasquali, M. Pedio, G. Selvaggi, G. Naletto, M. G. Pelizzo, and G. Tondello, *AIP Conf. Proc.* **705** (2004) 450–453.
25. N. Sadegh, Q. Evrard, P. M. Kraus, and A. M. Brouwer, *submitted* (2023)
26. B. L. Henke, E. M. Gullikson, and J. C. Davis, *At. Data Nucl. Data Tables* **55** (1993) 181.
27. N. Sadegh, M. van der Geest, J. Haitjema, F. Campi, S. Castellanos, P. M. Kraus, and A. M. Brouwer, *J. Photopolym. Sci. Technol.* **33** (2020) 145.
28. C. R. Arumainayagam, H.-L. Lee, R. B. Nelson, D. R. Haines, and R. P. Gunawardane, *Surf. Sci. Rep.* **65** (2010) 1.
29. J. Torok, R. Del Re, H. Herbol, S. Das, I. Bocharova, A. Paolucci, L. E. Ocola, C. Ventrice Jr, E. Lifshin, G. Denbeaux, and R. L. Brainard, *J. Photopolym. Sci. Technol.* **26** (2013) 625.
30. L.-L. Chua, M. Dipankar, S. Sivaramakrishnan, X. Gao, D. Qi, A. T. S. Wee, and P. K. H. Ho, *Langmuir* **22** (2006) 8587.
31. R. L. M. Gieseking, *Mater. Horiz.* **9** (2022) 25.
32. T. Okabe, *J. Phys. Soc. Jpn.* **35** (1973) 1496.
33. J. J. Ritsko, L. J. Brillson, R. W. Bigelow, and T. J. Fabish, *J. Chem. Phys.* **69** (1978) 3931.
34. H. Ahn, D. W. Oblas, and J. E. Whitten, *Macromolecules* **37** (2004) 3381.
35. R. Naaman, and L. Sanche, *Chem. Rev.* **107** (2007) 1553.
36. Y. Zheng, and L. Sanche, *Appl. Phys. Rev.* **5** (2018) 021302.
37. M. Pope, and C. E. Swenberg, *Electronic Processes in Organic Crystals and Polymers*, Oxford University Press, Oxford, **1999**.
38. M. Huttula, E. Kukk, S. Heinäsmäki, M. Jurvansuu, S. Fritzsche, H. Aksela, and S. Aksela, *Phys. Rev. A* **69** (2004) 012702.